

Design of broadband high-efficiency superconducting-nanowire single photon detectors

This content has been downloaded from IOPscience. Please scroll down to see the full text.

2016 Supercond. Sci. Technol. 29 065016

(<http://iopscience.iop.org/0953-2048/29/6/065016>)

View [the table of contents for this issue](#), or go to the [journal homepage](#) for more

Download details:

IP Address: 130.237.35.236

This content was downloaded on 26/05/2016 at 09:02

Please note that [terms and conditions apply](#).

Design of broadband high-efficiency superconducting-nanowire single photon detectors

L Redaelli^{1,2}, G Bulgarini³, S Dobrovolskiy³, S N Dorenbos³, V Zwiller^{1,2,4,5}, E Monroy^{1,2} and J M Gérard^{1,2}

¹ Univ. Grenoble Alpes, F-3800 Grenoble, France

² CEA, INAC-PHELIQS, Nanophysics and Semiconductors group, F-38000, Grenoble, France

³ Single Quantum B.V., 2628 CH Delft, The Netherlands

⁴ TU Delft, Kavli Institute of Nanosciences, 2628 CH Delft, The Netherlands

⁵ KTH Stockholm, Departement of Applied Physics, SE-114 28 Stockholm, Sweden

E-mail: luca.redaelli@cea.fr

Received 17 February 2016, revised 20 April 2016

Accepted for publication 21 April 2016

Published 6 May 2016



CrossMark

Abstract

In this paper several designs to maximize the absorption efficiency of superconducting-nanowire single-photon detectors are investigated. Using a simple optical cavity consisting of a gold mirror and a SiO₂ layer, the absorption efficiency can be boosted to over 97%: this result is confirmed experimentally by the realization of an NbTiN-based detector having an overall system detection efficiency of 85% at 1.31 μm . Calculations show that by sandwiching the nanowire between two dielectric Bragg reflectors, unity absorption (>99.9%) could be reached at the peak wavelength for optimized structures. To achieve broadband high efficiency, a different approach is considered: a waveguide-coupled detector. The calculations performed in this work show that, by correctly dimensioning the waveguide and the nanowire, polarization-insensitive detectors absorbing more than 95% of the injected photons over a wavelength range of several hundred nm can be designed. We propose a detector design making use of GaN/AlN waveguides, since these materials allow lattice-matched epitaxial deposition of Nb(Ti)N films and are transparent on a very wide wavelength range.

Keywords: photodetectors, single-photon detectors, superconducting-nanowire detectors, waveguide, microcavity, SNSPD, nitride

(Some figures may appear in colour only in the online journal)

1. Introduction

Highly efficient detection of single photons is of capital importance not only for advanced quantum optics experiments but, increasingly, for many emerging industrial applications [1, 2]. Single-photon detectors (SPDs) are used today in many fields, such as quantum key distribution [3, 4], time-of-flight depth ranging applications such as the Lidar [5, 6], space-to-ground optical communication [7], singlet oxygen detection for medical applications [8], and integrated circuit testing [9, 10].

In recent years, superconducting-nanowire single-photon detectors (SNSPDs) have undergone rapid development, and

they now outperform single-photon avalanche diodes in many insights [11, 12], especially in the infrared spectral range. Superior detection efficiencies, up to 93% [13–15], have been demonstrated with SNSPDs at telecom wavelength, which, combined with the very high detector speeds, make SNSPDs the ideal candidate for many of the aforementioned applications [16].

The overall system detection efficiency (η_{SDE}) of a SNSPD can be seen as the product of three contributions: the coupling efficiency (η_{coup}), the absorption efficiency (η_{abs}) and the internal efficiency (η_{int}) [1]: $\eta_{\text{SDE}} = \eta_{\text{coup}} \times \eta_{\text{abs}} \times \eta_{\text{int}}$.

The coupling efficiency η_{coup} is the probability that a photon travelling in the optical fiber carrying the signal is

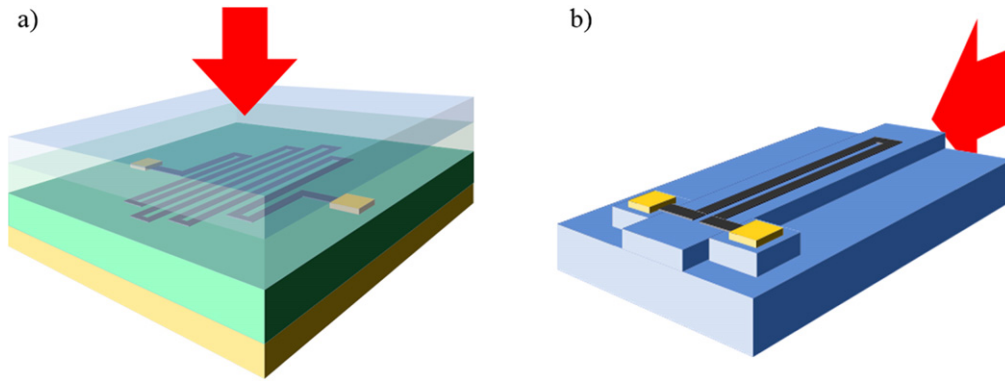


Figure 1. Schematic description of the device designs investigated in this paper. (a) Microcavity-enhanced detector: the nanowire meander (black) is sandwiched between two mirrors. One possible layer stack, depicted here as an example, is (starting from the bottom): a metal layer (e.g. Au, dark yellow in the figure), a transparent dielectric layer (e.g.: SiO₂, green in the figure), the nanowire meander, another dielectric layer (e.g. SiO₂, semitransparent-green layer) and a final layer consisting of higher-index dielectric (e.g. TiO₂, top semitransparent-blue layer). (b) Waveguide-coupled detector: The material in blue is a semiconductor or a dielectric which is transparent for the injected light. In both drawings, the superconducting nanowire is contacted by two metal pads (yellow squares), and red arrows indicate the direction of incidence of light.

coupled to the detector. The absorption efficiency η_{abs} provides a measure of the probability, for a photon impinging on the detector, to be actually absorbed by it rather than transmitted or reflected. Finally, the internal efficiency η_{int} is the probability of registering a voltage pulse at the nanowire leads when a photon is absorbed. This latter parameter depends on the choice and quality of the superconducting material, as well as on the nanowire width. A few years ago, high internal efficiencies approaching 100% at telecom wavelength were demonstrated with ultranarrow (30 nm) NbN nanowires [17]⁶. More recently reported values exceed 90% internal efficiency for 100 nm wide NbTiN nanowires [18], and reach 100% for comparably sized, or even wider, WSi [13] and MoSi [19, 20] nanowires. The optimization of η_{int} will, however, not be discussed in this paper.

The coupling efficiency, η_{coup} , is usually boosted by folding the detecting nanowire in a tightly packed meandering structure, covering a circular area several microns in diameter. It is then possible to efficiently couple the light output from a fiber to the center of the nanowire meander with a self-aligning method, achieving coupling efficiencies close to unity [21].

Achieving high absorption efficiency is often difficult in SNSPDs. Since the light is usually coupled vertically to the thin (4–8 nm) nanowire, only a small fraction of it is absorbed. Several techniques have been developed to enhance η_{abs} . In particular, two device designs have been proposed: the ‘microcavity-enhanced’ design, and the ‘waveguide-coupled’ (or ‘travelling-wave’) design. In microcavity-enhanced detectors, the meandering wire is enclosed in an optical cavity to enhance absorption (figure 1(a)) [13–15, 22–26]. Light can be injected from the front-side or through the substrate. In the waveguide approach the nanowire is patterned on top of a ridge-waveguide [19, 27–33]. The light is injected and

propagates in the waveguide, and the evanescent tail of the mode couples to the nanowire, eventually leading to complete absorption (figure 1(b)).

In this paper, both approaches will be studied by optical simulations, and their respective advantages and drawbacks will be discussed. First, the microcavity approach will be studied (section 2), with several designs of increasing complexity. For fabrication simplicity reasons, we choose to illuminate the device through the front-side. One of the designs has been realized experimentally and characterized, in order to validate the calculations. More complex cavity designs enabling absorption efficiencies close to unity will be then presented. Finally, high-efficiency polarization-insensitive detectors based on the waveguide-coupled design will be studied in section 3. An innovative device architecture will be proposed, in which the nanowire is deposited on an AlN/GaN waveguide.

2. Microcavity-enhanced detectors

2.1. Simulation method and optical model

In this section, devices based on the microcavity approach are studied by 2D finite-difference time-domain (FDTD) simulations using the commercial software *RSoft FullWAVE* [34]. The device is modeled as an infinite grating, as shown in figure 2(a). Only one grating period is drawn and calculated, and in-plane periodic boundary conditions are applied. The 2D analysis is justified because the photons are incoming at normal incidence and the wavefront can be approximated as planar: the grating period is much smaller than both the wavelength and the detector diameter. The top and bottom domain boundaries are 0.2 μm thick perfectly matched layers (PML). A nonuniform graded grid is used, in order to allow precise modeling of the thin nanowire but limit the overall calculation effort. The finest grid size, used at each layer boundary, is set to 1 nm in x direction, and to one tenth of the nanowire thickness (i.e. 0.7 nm) in z direction. The coarser

⁶ 100% internal efficiency is not explicitly claimed; however it is generally accepted that the saturation of the detection efficiency with increasing bias current, as observed in the reference, corresponds to an internal efficiency close to 100%.

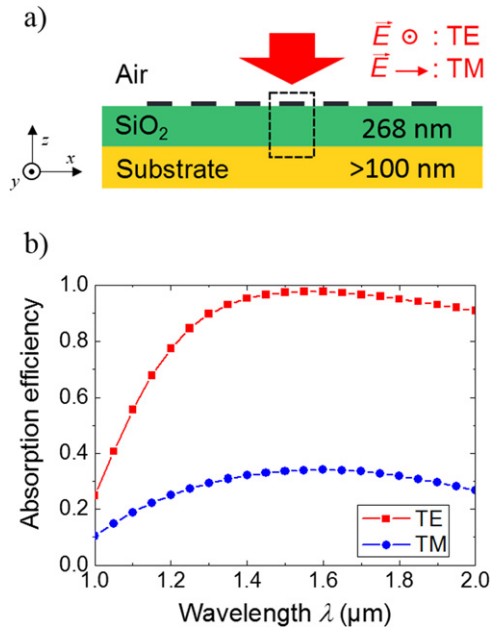


Figure 2. (a) Cross-section scheme of a ‘half-cavity’ detector design (not to scale). The area enclosed in the dashed rectangle corresponds to the simulated unit cell. The indicated layer thicknesses correspond to a device optimized for maximum TE absorption at a wavelength of $1.55 \mu\text{m}$. (b) Calculated absorption efficiency as a function of wavelength for the ‘half-cavity’ device shown in (a).

grid size is 10 nm, both in x and z . For simplicity, throughout this section we will refer to ‘TE-polarized light’ when the electric field is parallel to the nanowire length, ‘TM-polarized’ light for the opposite case, where the electric field is perpendicular to the nanowire.

The absorption efficiency is calculated, once the steady state is reached, by subtracting from the input power the power reaching the top PML boundary due to reflection, and the power absorbed by the backside mirror (if any). The thickness of the backside mirror is chosen so that the transmitted power reaching the bottom boundary is $<0.1\%$ of the input power.

The wavelength-dependent complex refractive indices used in the calculations were taken from value tables reported in literature. Their values at $1.55 \mu\text{m}$ are: $4.80 + i6.05$ for NbTiN [35]⁷, $4.58 + i3.66$ for WSi [13], 2.45 for TiO₂ [36–38], 1.44 for SiO₂, and $0.57 + i9.66$ for Au [39].

2.2. Results and discussion

The nanowire thickness is fixed to 7 nm, the width to 100 nm, and the spacing between two nearby nanowire meanders is set to 100 nm: values similar to these are typical for Nb(Ti)N based detectors [15, 40, 41]. In this configuration, assuming a semi-infinite SiO₂ layer, the calculated absorption probability would be as low as 29% for TE-polarized photons, and 11% for TM-polarized photons.

The absorption efficiency can be increased by placing a highly reflective mirror below the SiO₂ layer and reducing the

SiO₂ thickness close to a quarter of the wavelength, so that light coupling in the nanowire is enhanced by constructive interference. In the real device, which makes use of a gold mirror and is designed for operation at telecom wavelength ($1.55 \mu\text{m}$), the phase changes induced upon reflection at the metallic/dielectric interfaces, as well as the non-zero NbTiN thickness, place the optimum SiO₂ thickness value for maximum absorption at 268 nm. Figure 2(b) displays the absorption in the superconducting nanowire as a function of the incident wavelength considering TE- and TM-polarized light. In this case, 97.6% absorption efficiency for TE-polarized photons is achieved, whereas TM absorption is much less efficient, with a peak value of 37%. Note that the maximum achievable TE efficiency would be lower, if a superconducting material with lower absorption coefficient (e.g. WSi), a thinner nanowire, or a lower fill-factor (i.e. wider gaps between the wires) were used. For instance, replacing NbTiN with WSi, the maximum attainable TE efficiency would be 91.5%, for an optimum SiO₂ thickness of 229 nm. If the nanowire geometry of the record-holding reference [13] is used instead (WSi wire, thickness 4.3 nm, width 102 nm, pitch 200 nm) the maximum TE efficiency would be 70.1% (TM efficiency 41.0%), for a SiO₂ thickness of 231 nm.

To validate these calculations, a device using the ‘half-cavity’ geometry of figure 2(a) was fabricated and characterized by the company *Single Quantum*. A silicon wafer was used as substrate and mechanical support. The 7 nm thick NbTiN film was deposited on SiO₂ by magnetron sputtering and patterned into a nanowire meander (wire width 100 nm, pitch 200 nm) by e-beam lithography and Reactive Ion Etching (RIE). A hydrogen silsesquioxane mask was used, and RIE was performed in SF₆/O₂ atmosphere. In order to boost the optical absorption at $1.31 \mu\text{m}$, the superconducting nanowire was positioned on top of a 230 nm thick SiO₂ layer and a gold mirror. Dicing was performed by deep RIE (‘Bosch etching’) and cleaving. The nanowire meander was aligned to the core of a single-mode fiber using a fiber alignment sleeve, a technique similar to the one described in reference [21]. Finally, the chip was mounted on a printed circuit board and wire-bonded.

The detection efficiency was measured at a temperature of 2.5 K in a closed-cycle cryostat. As photon source a *Fianium Supercontinuum Laser SC-400-4* with acousto-optic tunable filters was used; the optical pulses were attenuated by a *JDS Uniphase JDSU HA9* calibrated programmable attenuator, and the photon polarization was controlled by a *Thorlabs FPC561 Fiber Polarization Controller*. Electrical amplification of the detection pulses and counting were performed with a *Single Quantum* proprietary driver, while optical power measurements were performed by a *Thorlabs Digital Optical Power and Energy Meter PM100D* equipped with a *Thorlabs S154C* InGaAs photodiode. The measurement values at $1.31 \mu\text{m}$, wavelength at which the structure was optimized to operate, were 10 nW average laser power with an additional attenuation of 50 dB, which correspond to a photon flux of 6.59×10^5 photons s⁻¹.

⁷ For wavelengths exceeding $1.68 \mu\text{m}$, the n and k values are linearly extrapolated (up to $2.0 \mu\text{m}$). This is a reasonable approximation, since most metals show a linear-like increase of their refractive index in this range.

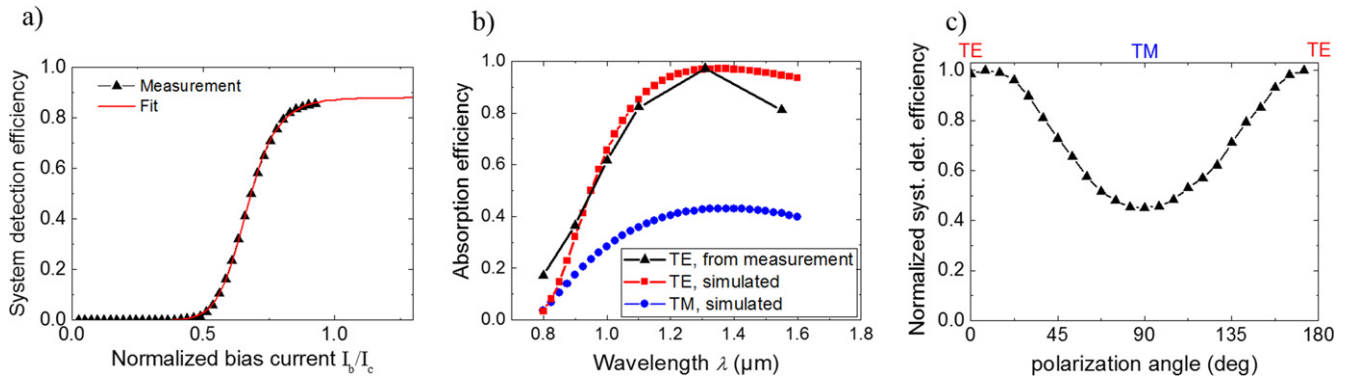


Figure 3. (a) System detection efficiency (η_{SDE}) measured at $1.31 \mu\text{m}$ of a half-cavity device incorporating a gold mirror and a 230 nm thick SiO₂ layer. The efficiency is plotted as a function of the normalized bias current, showing saturation of the detection efficiency when approaching the critical current I_c . The maximum system detection efficiency is 85.6%. (b) Wavelength-dependent absorption efficiency compared to simulation. The experimental absorption efficiency is calculated from the measured η_{SDE} by dividing the experimental values by the estimated η_{int} and η_{coup} . (c) Dependence of the detection efficiency on the polarization angle, normalized to the peak TE absorption efficiency.

The measurements results are shown in figures 3(a) and (b), together with the simulated absorption efficiency curves. In figure 3(a) the system detection efficiency at $1.31 \mu\text{m}$ is plotted as a function of the normalized bias current I_b/I_c , where I_b is the bias current and I_c the critical current, defined as the current which causes the nanowire to transition to the normal state in absence of illumination. The peak system detection efficiency η_{SDE} reaches⁸ $85.6\% \pm 4.7\%$, which is, to the best of our knowledge, the highest reported to date for Nb(Ti)N-based SNSPDs. The efficiency is almost saturated; by fitting the curve with a sigmoidal function (logistic function), and assuming that η_{int} would be 100% at saturation, as in [18], we obtain that the maximum measured value of η_{int} is 97.4%. From these values of η_{SDE} and η_{int} , and from the calculated $\eta_{\text{abs}} = 97.0\%$, the coupling efficiency can be estimated as $\eta_{\text{coup}} = 89.3\%$. This value is lower than the value $\eta_{\text{coup}} > 99\%$ obtained in [21]. However, additional coupling losses due to defects at the fiber ferrule facets, or a small imperfection in one of the process steps (etching, aligning, gluing...) could easily account for the missing photons.

In order to compare experimental measurements and simulations, we assume that the coupling efficiency and the internal efficiency are constant across the considered wavelength range, and independent from light polarization. We can thus divide the experimental values by the estimated η_{int} and η_{coup} and compare the obtained curve to the theoretically calculated absorption efficiency versus wavelength curve in figure 3(b). The good agreement of the experimental wavelength dependence with the simulation confirms that our model predicts accurately the spectral dependence of the SNSPDs under investigation. It is worth noting that, in figure 3(b), the experimental measurement drops significantly below the calculated efficiency value at $1.55 \mu\text{m}$, which might be partly explained by a non-saturated internal efficiency, i.e. our assumption of a constant η_{int} is not valid for wavelengths

larger than $1.31 \mu\text{m}$. Figure 3(c) shows the typical system detection efficiency of a half-cavity device as a function of the light polarization angle. By normalizing the peak value to the TE absorption efficiency, we observe that the minimum efficiency well matches the simulated TM value, thus validating the calculation predictions.

It is possible to further increase the absorption efficiency of the devices by adding a matching dielectric mirror on the device front side, thereby completing the optical cavity, as done for example in [13]. Two different geometries leaning on this concept are depicted in figures 4(a) and (c), and will be studied in the following paragraphs. By optimizing the thickness of the dielectric layers, the reflected power can be reduced close to zero thanks to destructive interference, so that all the power is absorbed inside the cavity (i.e., $\eta_{\text{abs}} \sim 1$). If the backside reflector is a gold mirror and the previously introduced nanowire meander sizes are used, the maximum efficiency that can be achieved is 98.6%. In order to achieve unity efficiency ($>99.9\%$) the Au mirror must be replaced by a dielectric Bragg mirror, since Au is not a perfect reflector at $1.55 \mu\text{m}$ —it absorbs at least 1%–2% of the incident radiation. In figure 4 both cavity configurations are illustrated, and the respective calculated absorption efficiencies are plotted as a function of wavelength and polarization. In comparison to the half-cavity configuration in figure 2, TM absorption is enhanced, but the absorption peak is red shifted with respect to the TE absorption peak. By tuning the front mirror and spacer thicknesses, it is possible to design a polarization-independent detector, although this will come at the cost of peak efficiency. For example, calculations show that for front mirror thicknesses of 263 nm (TiO₂) and 89 nm (SiO₂), the absorption efficiency would be of 80% for both polarizations. Considering the full-cavity detectors of figure 4, precise control of the dielectric layer thicknesses is capital to attain such high absorption efficiencies. We assume a thickness tolerance of $\pm 2\%$, a realistic number for modern deposition techniques, and calculate its impact on the peak TE absorption efficiency. We find out that, in the worst-case scenario (all dielectric layers are 2% thinner than expected), such a

⁸ The error of the system detection efficiency is given by the root mean square of the power meter and the optical attenuator accuracies. The instrument errors as specified by the manufacturers are used.

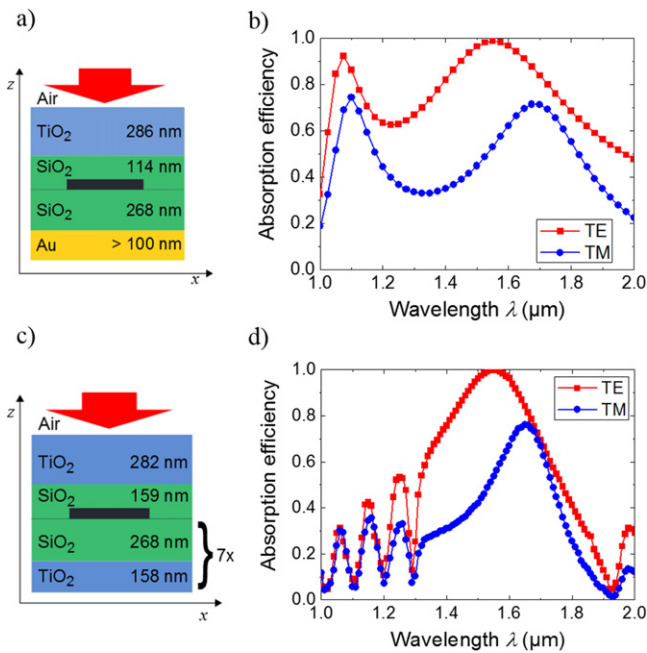


Figure 4. Microcavity detectors optimized for high TE absorption efficiency at $1.55 \mu\text{m}$: (a) and (b) full-cavity design with backside Au mirror, (c) and (d) full-cavity with backside Bragg mirror. (a) and (c) Illustrations (not to scale) of the simulated unit cells, together with (b) and (d) the respective efficiencies calculated as a function of wavelength and polarization.

variation would cause the peak efficiency of the design in figure 4(a) to drop from 98.6% to 97.8%, while in the Bragg-backmirror design of figure 4(c) the efficiency would drop from above 99.9% to 98.0%.

In these ‘full-cavity’ configurations, peak efficiencies close to unity can be reached at any targeted wavelength and photon polarization, almost independent of the superconducting nanowire and of the nanowire size and absorption coefficient, by tuning the reflectivity of the front mirror. Even a non-optimum thickness of the first SiO₂ layer below the nanowire can be in most cases compensated by the front mirror design. This fact opens up novel interesting opportunities from a fabrication point of view, concerning the design in figure 4(a). Devices from the same wafer could be tuned to maximize the response at different wavelengths (or photon polarizations) at the end of the fabrication process, by fabricating front mirrors having different SiO₂ and TiO₂ thicknesses.

Microcavity-enhanced detectors are intrinsically wavelength sensitive, since they make use of interference effects to enhance absorption. When using a simple backside mirror (half-cavity, figure 2), the detection band is quite broad, with a $0.7 \mu\text{m}$ wide wavelength range around the peak (from 1.3 to $1.8 \mu\text{m}$) where $\eta_{\text{abs}} > 90\%$. When incorporating a front mirror (figure 4(a)), on the other hand, the detection band where $\eta_{\text{abs}} > 90\%$ is less than $0.2 \mu\text{m}$ wide (from about 1.45 to $1.65 \mu\text{m}$), and it shrinks even further when using a backside Bragg mirror.

In order to achieve polarization-insensitive and broadband detectors, a change of paradigm is necessary. A possible

approach is the waveguide-coupled detector design, which will be discussed in the next section.

3. Waveguide-coupled detectors

3.1. Detector design options

Various substrate/waveguide material combinations have been proposed for the realization of waveguide-coupled SNSPDs. The most obvious choice is silicon-on-insulator (SOI), in order to integrate this detector technology on-chip with photonic circuits working at telecom wavelength. Silicon waveguides rely on a very mature technology, with extremely low propagation losses [42]. Furthermore, the index difference between silicon and the underlying SiO₂ cladding is very high (about 2), and the mode can be tightly confined in very thin waveguides, providing intense evanescent field. This, in turn, allows for efficient evanescent coupling to the nanowire and highly efficient absorption, even in short waveguides: attenuations up to $1 \text{ dB } \mu\text{m}^{-1}$ have been demonstrated [31]. The main drawback of this technology is that silicon is not transparent below $1.1 \mu\text{m}$, so that it is not suitable e.g. for 850 nm fiber-optics transmission or for truly broadband detectors.

Other approaches include GaAs/AlGaAs [28] and Si₃N₄/SiO₂ [27] waveguides. In both cases the index difference is much lower than for SOI, which means that the mode confinement is less effective. Therefore, thicker and wider waveguides are needed to guide the mode, and its evanescent field will be less intense, so that longer detectors are necessary to achieve absorption efficiencies close to unity. The GaAs absorption edge is located around $0.9 \mu\text{m}$, which allows only slightly larger bandwidth than with silicon, while high-quality Si₃N₄ can have a much wider transparent band.

In this work we propose waveguide-coupled detectors fabricated on GaN/AlN waveguides, since this material system has some important advantages: AlN is lattice-matched to Nb(Ti)N, offering the best possible substrate for the deposition of high-quality superconducting films [43]. Furthermore, AlN and GaN are transparent over a very large band, from 0.4 to about $7.4 \mu\text{m}$ [44]: this opens the way to the design of detectors which can operate with high efficiency on a very broad wavelength range. The ridge-waveguide design is illustrated in figure 5(a). It consists of a double GaN/AlN waveguiding layer on a sapphire substrate. In this configuration, the mode maximum can be efficiently confined in the upper GaN layer. Sapphire acts as a cladding layer, thanks to the larger index difference with AlN (at $1.55 \mu\text{m}$, sapphire 1.75 [36, 45], AlN 2.12 [36, 46]) and GaN (2.32 [36, 47]). The thick AlN layer is needed as a buffer in order to achieve high crystalline quality in the upper GaN layer, where the maximum mode intensity propagates, and has a thickness of $1.1 \mu\text{m}$. Besides, the overall thicker waveguiding layers should facilitate fiber-waveguide coupling. A cleaved waveguide facet is shown in figure 5(b). In this sample, the waveguide was etched by inductive coupled plasma (ICP) RIE in GaN/AlN ($0.6 \mu\text{m}/1.1 \mu\text{m}$) layers grown by molecular beam epitaxy on a sapphire substrate. The etch depth is

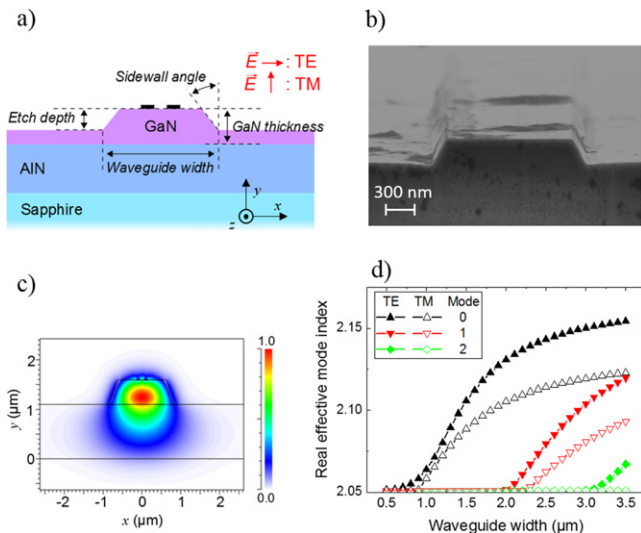


Figure 5. (a) Illustration of the waveguiding structure in cross-section (not to scale). The labels in *italics* indicate the most important parameters that will be optimized in the following. Note that the sidewall angle is defined so that a perfectly vertical sidewall would have a 0° angle. (b) SEM micrograph of a GaN/AlN ridge-waveguide. (c) Calculated fundamental TE mode for GaN thickness = etch depth = $0.5 \mu\text{m}$, sidewall angle = 25° . The field intensity is normalized to 1, 0 meaning absence of field, 1 maximum intensity. (d) Effective index of the first three TE and TM modes as a function of waveguide width (same waveguide geometry as before). The waveguide supports only the fundamental TE and TM mode for widths between 1 and $2 \mu\text{m}$.

here $0.35 \mu\text{m}$, the sidewall angle about 25° . The smooth facet is obtained by manually cleaving the sample along the natural GaN cleaving plane (*m*-plane). In order to obtain controlled cleaving, the sapphire substrate was preventively sawn to a predefined depth along the future cleaving line.

3.2. Simulation method and optical model

In order to quantify the absorption efficiency, we calculate the mode profile and complex effective index using a Finite Element (FEM) mode solver (RSoft FemSIM [34]), as shown in figure 5(c). The nanowire absorption is calculated from the imaginary part of the complex effective mode index. This method does not take into account the mode reflection at the nanowire onset, nor the additional absorption by the short transversal wire segment connecting the two parallel wire segments. This approximation is justified by the fact that the contribution of both effects is negligible, as pointed out in [31] and confirmed by a 3D FDTD simulation performed by the authors, in which these contributions were smaller than the numerical noise level of the simulation.

The nonuniform graded mesh is chosen so that the finest mesh size is ten times smaller than the smallest structure, both in *x* and *y* directions (0.7 nm in *x*, 10 nm in *y*). A coarser mesh is used ($0.02 \mu\text{m}$) where the material is uniform, far away from the material interfaces. The nanowire dimensions and spacing are unchanged from the microcavity design in section 2 (7 nm thick and 100 nm wide nanowire, with 100 nm spacing). Throughout this section we will refer to ‘TE-polarized’ light when the electric field vector is parallel

to the *x* direction (horizontal in figure 5(a)), ‘TM-polarized’ light when the electric field vector is parallel to the *y* direction (vertical in figure 5(a)).

The goal of the simulations is to optimize the waveguide dimensions in order to ensure single-mode operation and maximize the modal absorption. The most important parameters are highlighted in figure 5(a): the waveguide width and thickness, the waveguide etch depth, and the sidewall angle. Finally, the minimum waveguide length necessary to achieve unity absorption will be determined, considering the impact of the mode propagation losses.

3.3. Results and discussion

First, we define the maximum waveguide width which only supports the fundamental TE and TM modes by considering the evolution of the effective mode index as a function of waveguide width, as plotted in figure 5(d). We consider that a mode is supported when its effective index clearly rises above the index of the substrate modes and it is fully contained into the simulation domain (no variation of the index when enlarging the simulation domain). It is important to note that there is no sharp cutoff wavelength, since the modes slowly migrate from the substrate to the waveguide with increasing waveguide width. Below a waveguide width of $0.5 \mu\text{m}$, the waveguide does not support any mode, only substrate modes exist. Between 1 and $2 \mu\text{m}$, the fundamental TE and TM modes are supported. Above $2 \mu\text{m}$, the first order modes (TE first, then TM) start to appear. Thus, we choose $2 \mu\text{m}$ as the upper limit for the waveguide width.

The various waveguide dimensions (waveguide width, GaN thickness, etch depth, and sidewall angle) are then investigated in order to maximize absorption. In figures 6(a) and (b) the modal absorption of the fundamental TE and TM modes is plotted as a function of the waveguide width and the GaN thickness, respectively. Since TE absorption is consistently lower than TM absorption, the primary goal is to maximize TE absorption. The optimum is reached for a waveguide width of $1.7 \mu\text{m}$ and a GaN thickness of $0.5 \mu\text{m}$. If the waveguide size is smaller, the maximum mode intensity is pushed down in the AlN layer, and the intensity of the evanescent mode tail drops, i.e. the modal absorption drops. If, on the contrary, the waveguide is too large, the mode is more tightly confined in the GaN layer, thus reducing the evanescent tail intensity.

In figures 6(c) and (d) the waveguide etch depth and its sidewall angle are investigated. Deeper waveguides offer better lateral confinement, thus more intense evanescent field, up to an etch depth of $0.8 \mu\text{m}$. The sidewall slope has almost no impact on the modal absorption, up to an angle of 35° (figure 6(d)). On the other hand, a deeper etch would also increase the propagation losses, due to the increased interaction of the mode with the rough etched sidewalls. The sidewall angle is indirectly linked with the propagation losses, as well: the choice of the ICP-RIE etching parameters influences both the surface roughness and the sidewalls slope. Therefore, before choosing etch depth and angle, the impact of the waveguide losses on the device efficiency should be estimated. In this work we arbitrarily decide to stop the

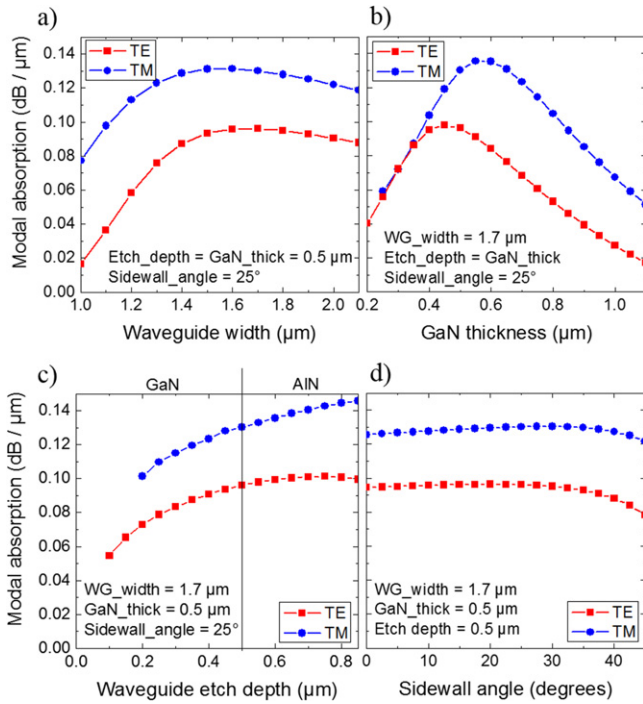


Figure 6. The modal absorption coefficient (in $\text{dB } \mu\text{m}^{-1}$) is plotted as a function of the waveguide width (WG_width) (a), GaN thickness (GaN_thick) (b), waveguide etch depth (Etch_depth) (c), and waveguide sidewall angle (Sidewall_angle) (d). Each time, only one parameter is varied; the three other parameters are fixed and their values are indicated in each plot. In (a) and (b) Etch_depth = GaN_thick, i.e. the waveguide is etched down till the GaN/AIN interface.

etching at the GaN/AIN interface (etch depth = $0.5 \mu\text{m}$), where TE absorption starts to saturate, and consider a 25° sidewall angle, as obtained experimentally in figure 5(b).

For a bare waveguide structure as the one considered here, propagation losses of about 2 dB mm^{-1} (4 dB mm^{-1}) or lower have been reported for TE (TM) polarization [48, 49]. These values correspond to 2.1% (3.1%) of the TE (TM) peak modal absorption induced by the NbTiN nanowire, which is $0.096 \text{ dB } \mu\text{m}^{-1}$ ($0.130 \text{ dB } \mu\text{m}^{-1}$). As a consequence, the maximum TE (TM) absorption efficiency will be limited at 97.9% (96.9%) for an infinite waveguide length. In figure 7(a) the attenuation of the TE and TM fundamental modes, propagating in the waveguide, is plotted as a function of the waveguide length L . The power drops to 0.1% of the input power (-30 dB attenuation) for $L = 306 \mu\text{m}$, i.e. an absorption efficiency of about 97.8% is achieved. TM attenuation, for the same L , is -10 dB larger, thus the maximum TM absorption efficiency of 96.9% is (almost) reached.

In figure 7(b), the absorption efficiency of the fundamental TE and TM modes is plotted as a function of wavelength. The curves are calculated for $L = 306 \mu\text{m}$, assuming that the waveguide losses are equal to 2 dB mm^{-1} for TE and 4 dB mm^{-1} for TM across the whole wavelength range. It should be noted that, for wavelengths shorter than $1.2 \mu\text{m}$ ($1.3 \mu\text{m}$), the first-order TE (TM) mode is supported. As a consequence, when coupling light into the waveguide, there is

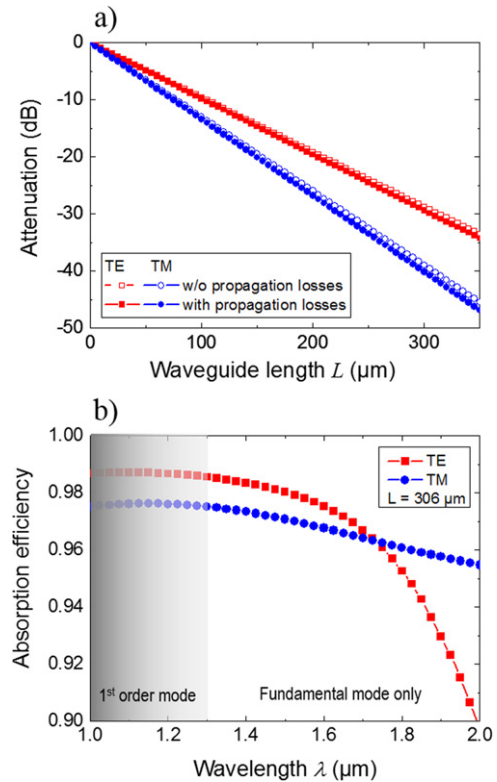


Figure 7. (a) Mode attenuation as a function of the waveguide length. (b) Absorption efficiency (net of waveguide losses) as a function of wavelength. Constant losses of 2 dB mm^{-1} (4 dB mm^{-1}) for TE (TM) radiation are considered. Note that the y axis starts at 0.9, and not 0 as in figure 4. Below $1.3 \mu\text{m}$ the graph is greyed out since part of the light might be injected in the first-order mode, resulting in an overestimation of the absorption efficiency.

an increasing probability that a fraction of the power will be injected into the first-order mode, which is poorly coupling to the nanowire, i.e. the absorption efficiency below $1.3 \mu\text{m}$ might be overestimated. Nevertheless, comparing figure 7(b) to figures 4(b) and (d), it can be stated that the waveguide approach offers high efficiencies, nearly independent on polarization, across a wavelength range which is potentially much larger than the one of microcavity-enhanced detectors.

A major drawback of the waveguide-coupled device design is that, in order to achieve high coupling efficiency, extremely precise alignment of the fiber and the waveguide is needed. Here, the simple fiber self-aligning method developed for normal-incidence detectors described in [21] cannot be used. This is not an issue when thinking of waveguide-coupled detectors for integration in photonic circuits, where both the photon source and the detector are on the same chip: on-chip photonics is indeed a major application field for this kind of detectors, and has been motivating their development in the first place [18, 27–33, 41]. On the other hand, if the goal is the fabrication of a stand-alone detector for other industrial applications, the overall detector efficiency will be necessarily limited by the fiber-waveguide coupling efficiency. Coupling losses below 1 dB can be achieved, and have been realized on Si CMOS technology [50], but they require complex and expensive alignment systems. The task is made even more

difficult for SNSPDs, since they operate at cryogenic temperatures, and the induced mechanical strain due to thermal mismatch during cooling needs to be managed.

Finally, for applications where large coupling losses (i.e. low system detection efficiencies) are acceptable, but detector speed, polarization insensitivity, and/or broadband operation are essential, the waveguide approach might be interesting. Since the absorption efficiency depends logarithmically on the nanowire length, devices with short nanowires, i.e. shorter dead times and higher detection rates, can be designed. An interesting ‘hybrid’ approach, combining waveguide-coupling and cavity effects has been recently proposed [41], in which high absorption efficiencies are achieved using ultrashort nanowires.

4. Conclusion

In this paper, different ways to enhance the absorption efficiency of SNSPDs have been investigated by optical simulations. Two main approaches have been discussed: the microcavity-enhanced device, where light absorption is boosted by embedding the superconducting nanowire meander in an optical cavity, and the waveguide-coupled device, where the evanescent tail of the mode is coupled to a nanowire deposited on top of the waveguiding structure.

The simplest microcavity design makes use of a backside gold mirror and a SiO₂ dielectric layer to enhance absorption in the 7 nm thick NbTiN nanowire through constructive interference. High absorption efficiencies of 97.6% can be achieved at 1.55 μm , but only for linearly polarized light where the electric field oscillates parallel to the nanowire segments. A detector based on this architecture has been realized and characterized, and the measurements are consistent with the simulation results (peak system detection efficiency of 85% at 1.31 μm).

By adding a front dielectric mirror to complete the vertical cavity, an absorption efficiency of 98.6% can be achieved at 1.55 μm . This value can be further increased to over 99.9% by replacing the backside Au mirror with a dielectric Bragg mirror. In both cases, the TE/TM polarization absorption ratio is between 1.4 and 1.7 but, by tuning the front mirror layer thicknesses, it is possible to reach a compromise and achieve detectors which are polarization-insensitive at 1.55 μm and have around 80% absorption efficiency.

Concerning the waveguide-coupled approach, realization on a GaN/AlN waveguide has been proposed as a good candidate for on-chip photonics applications. In this configuration, highly efficient and almost polarization-insensitive photon absorption over a very broad wavelength range is possible. The detector is designed to absorb over 97% of both TE- and TM-polarized photons at 1.55 μm , and over 90% of the photons over a wavelength range of more than 700 nm.

Acknowledgments

This work was funded by The European Commission via the Marie Skłodowska Curie IF grant ‘SuSiPOD’ (H2020-

MSCA-IF-2015, #657497), the French National Research Agency via the ‘WASI’ (ANR-14-CE26-0007) and ‘GANEX’ (ANR-11-LABX-0014) programs, and the Grenoble Nanosciences Foundation.

References

- [1] Natarajan C M, Tanner M G and Hadfield R H 2012 Superconducting nanowire single-photon detectors: physics and applications *Supercond. Sci. Technol.* **25** 063001
- [2] Hadfield R H 2009 Single-photon detectors for optical quantum information applications *Nat. Photon.* **3** 696–705
- [3] Gisin N, Ribordy G, Tittel W and Zbinden H 2002 Quantum cryptography *Rev. Mod. Phys.* **74** 145–95
- [4] Choi I *et al* 2014 Field trial of a quantum secured 10 Gb s⁻¹ DWDM transmission system over a single installed fiber *Opt. Express* **22** 23121
- [5] Zhou H, He Y, You L, Chen S, Zhang W, Wu J, Wang Z and Xie X 2015 Few-photon imaging at 1550 nm using a low-timing-jitter superconducting nanowire single-photon detector *Opt. Express* **23** 14603
- [6] McCarthy A, Krichel N J, Gemmell N R, Ren X, Tanner M G, Dorenbos S N, Zwiller V, Hadfield R H and Buller G S 2013 Kilometer-range, high resolution depth imaging via 1560 nm wavelength single-photon detection *Opt. Express* **21** 8904
- [7] Grein M E *et al* 2011 Design of a ground-based optical receiver for the lunar laser communications demonstration *Proc. IEEE Int. Conf. on Space Optical Systems and Applications (IEEE)* pp 78–82
- [8] Gemmell N R, McCarthy A, Liu B, Tanner M G, Dorenbos S D, Zwiller V, Patterson M S, Buller G S, Wilson B C and Hadfield R H 2013 Singlet oxygen luminescence detection with a fiber-coupled superconducting nanowire single-photon detector *Opt. Express* **21** 5005
- [9] Shehata A B, Stellari F, Weger A, Song P, Anant V, Sunter K, Berggren K K, Lundquist T and Ramsay E 2014 Ultra-low voltage TRE measurements from 32 nm SOI CMOS integrated circuits *Proc. 40th Int. Symp. for Testing and Failure Analysis (ASM International)* pp 415–21
- [10] Shehata A B and Stellari F 2015 Tuning of superconducting nanowire single-photon detector parameters for VLSI circuit testing using time-resolved emission *Proc. SPIE* **9370** 93702Z
- [11] Tosi A, Calandri N, Sanzaro M and Acerbi F 2014 Low-noise, low-jitter, high detection efficiency InGaAs/InP single-photon avalanche diode *IEEE J. Sel. Top. Quantum Electron.* **20** 192–7
- [12] Scarcella C, Boso G, Ruggeri A and Tosi A 2015 InGaAs/InP single-photon detector gated at 1.3 GHz with 1.5% afterpulsing *IEEE J. Sel. Top. Quantum Electron.* **21** 17–22
- [13] Marsili F *et al* 2013 Detecting single infrared photons with 93% system efficiency *Nat. Photon.* **7** 210–4
- [14] Rosenberg D, Kerman A J, Molnar R J and Dauler E A 2013 High-speed and high-efficiency superconducting nanowire single photon detector array *Opt. Express* **21** 1440–7
- [15] Miki S, Yamashita T, Terai H and Wang Z 2013 High performance fiber-coupled NbTiN superconducting nanowire single photon detectors with Gifford-McMahon cryocooler *Opt. Express* **21** 10208–14
- [16] Dauler E A, Grein M E, Kerman A J, Marsili F, Miki S, Nam S W, Shaw M D, Terai H, Verma V B and Yamashita T 2014 Review of superconducting nanowire single-photon detector system design options and demonstrated performance *Opt. Eng.* **53** 081907

- [17] Marsili F, Najafi F, Dauler E, Bellei F, Hu X, Csete M, Molnar R J and Berggren K K 2011 Single-photon detectors based on ultranarrow superconducting nanowires *Nano Lett.* **11** 2048–2053
- [18] Waki K, Yamashita T, Inoue S, Miki S, Terai H, Ikuta R, Yamamoto T and Imoto N 2015 Fabrication and characterization of superconducting nanowire single-photon detectors on Si waveguide *IEEE Trans. Appl. Supercond.* **25** 1–4
- [19] Korneeva Y P, Mikhailov M Y, Pershin Y P, Manova N N, Divochiy A V, Vakhtomin Y B, Korneev A A, Smirnov K V, Devizenko A Y and Goltsman G N 2014 Superconducting single-photon detector made of MoSi film *Supercond. Sci. Technol.* **27** 095012
- [20] Verma V B *et al* 2015 High-efficiency superconducting nanowire single-photon detectors fabricated from MoSi thin-films *Opt. Express* **23** 33792–801
- [21] Miller A J, Lita A E, Calkins B, Vayshenker I, Gruber S M and Nam S W 2011 Compact cryogenic self-aligning fiber-to-detector coupling with losses below one percent *Opt. Express* **19** 9102–10
- [22] Tanner M G *et al* 2010 Enhanced telecom wavelength single-photon detection with NbTiN superconducting nanowires on oxidized silicon *Appl. Phys. Lett.* **96** 221109
- [23] Miki S, Takeda M, Fujiwara M, Sasaki M and Wang Z 2009 Compactly packaged superconducting nanowire single-photon detector with an optical cavity for multichannel system *Opt. Express* **17** 23557
- [24] Baek B, Stern J A and Nam S W 2009 Superconducting nanowire single-photon detector in an optical cavity for front-side illumination *Appl. Phys. Lett.* **95** 191110
- [25] Anant V, Kerman A J, Dauler E A, Yang J K W, Rosfjord K M and Berggren K K 2008 Optical properties of superconducting nanowire single-photon detectors *Opt. Express* **16** 10750
- [26] Rosfjord K M, Yang J K W, Dauler E A, Kerman A J, Anant V, Voronov B M, Goltsman G N and Berggren K K 2006 Nanowire single-photon detector with an integrated optical cavity and anti-reflection coating *Opt. Express* **14** 527
- [27] Kahl O, Ferrari S, Kovalyuk V, Goltsman G N, Korneev A and Pernice W H P 2015 Waveguide integrated superconducting single-photon detectors with high internal quantum efficiency at telecom wavelengths *Sci. Rep.* **5** 10941
- [28] Sahin D *et al* 2015 Waveguide nanowire superconducting single-photon detectors fabricated on GaAs and the study of their optical properties *IEEE J. Sel. Top. Quantum Electron.* **21** 1–10
- [29] Najafi F *et al* 2015 On-chip detection of non-classical light by scalable integration of single-photon detectors *Nat. Commun.* **6** 5873
- [30] Schuck C, Pernice W H P and Tang H X 2013 NbTiN superconducting nanowire detectors for visible and telecom wavelengths single photon counting on Si₃N₄ photonic circuits *Appl. Phys. Lett.* **102** 051101
- [31] Sahin D *et al* 2013 Waveguide photon-number-resolving detectors for quantum photonic integrated circuits *Appl. Phys. Lett.* **103** 111116
- [32] Pernice W H P, Schuck C, Minaeva O, Li M, Goltsman G N, Sergienko A V and Tang H X 2012 High-speed and high-efficiency travelling wave single-photon detectors embedded in nanophotonic circuits *Nat. Commun.* **3** 1325
- [33] Sprengers J P *et al* 2011 Waveguide single-photon detectors for integrated quantum photonic circuits *Appl. Phys. Lett.* **99** 181110
- [34] RSoft Photonic Design software, Synopsys® (<http://optics.synopsys.com/rsoft/>)
- [35] Dorenbos S N 2011 Superconducting single photon detectors *PhD Dissertation* Technische Universiteit Delft
- [36] Online database (<http://refractiveindex.info>)
- [37] Kischkat J *et al* 2012 Mid-infrared optical properties of thin films of aluminum oxide, titanium dioxide, silicon dioxide, aluminum nitride, and silicon nitride *Appl. Opt.* **51** 6789–98
- [38] DeVore J R 1951 Refractive indices of rutile and sphalerite *J. Opt. Soc. Am.* **41** 416–9
- [39] RSoft CAD Refractive index value provided by the built-in database of the simulation software (<https://optics.synopsys.com/rsoft/>)
- [40] Dorenbos S N, Reiger E M, Perinetti U, Zwiller V, Zijlstra T and Klapwijk T M 2008 Low noise superconducting single photon detectors on silicon *Appl. Phys. Lett.* **93** 131101
- [41] Akhlaghi M K, Schelew E and Young J F 2015 Waveguide integrated superconducting single-photon detectors implemented as near-perfect absorbers of coherent radiation *Nat. Commun.* **6** 8233
- [42] Li G *et al* 2012 Ultralow-loss, high-density SOI optical waveguide routing for macrochip interconnects *Opt. Express* **20** 12035
- [43] Sam-Giao D, Pouget S, Bougerol C, Monroy E, Grimm A, Jebari S, Hofheinz M, Gérard J-M and Zwiller V 2014 High-quality NbN nanofilms on a GaN/AlN heterostructure *AIP Adv.* **4** 107123
- [44] Beeler M, Trichas E and Monroy E 2013 III-nitride semiconductors for intersubband optoelectronics: a review *Semicond. Sci. Technol.* **28** 074022
- [45] Dodge M J 1986 Refractive index *Handbook of Laser Science and Technology* vol IV Optical Materials: Part 2 Properties ed M J Weber (Boca Raton, FL: CRC Press)
- [46] Pastrňák J and Roskocová L 1966 Refraction index measurements on AlN single crystals *Phys. Status Solidi b* **14** K5–8
- [47] Barker A S and Ilegems M 1973 Infrared lattice vibrations and free-electron dispersion in GaN *Phys. Rev. B* **7** 743–50
- [48] Li W, Luo Y, Xiong B, Sun C, Wang L, Wang J, Han Y, Yan J, Wei T and Lu H 2015 Fabrication of GaN-based ridge waveguides with very smooth and vertical sidewalls by combined plasma dry etching and wet chemical etching *Phys. Status Solidi a* **212** 2341–44
- [49] Li Y, Bhattacharyya A, Thomidis C, Moustakas T D and Paiella R 2007 Nonlinear optical waveguides based on near-infrared intersubband transitions in GaN/AlN quantum wells *Opt. Express* **15** 5860
- [50] Shoji T, Tsuchizawa T, Watanabe T, Yamada K and Morita H 2002 Low loss mode size converter from 0.3 μm square Si wire waveguides to singlemode fibres *Electron. Lett.* **38** 1669